ESCRT-III and ER–PM contacts maintain lipid homeostasis

Jeff R. Jorgensen[a], Reika Tei[a], Jeremy M. Baskin[a], Agnès H. Michel[b], Benoît Kornmann[b], and Scott D. Emr[a,*]

[a]Weill Institute for Cell and Molecular Biology and Department of Molecular Biology and Genetics, Cornell University, Ithaca, NY 14853; [b]Department of Biochemistry, University of Oxford, Oxford OX1 3QU, United Kingdom

ABSTRACT **Eukaryotic cells are compartmentalized into organelles by intracellular membranes. While the organelles are distinct, many of them make intimate contact with one another. These contacts were first observed in the 1950s, but only recently have the functions of these contact sites begun to be understood. In yeast, the endoplasmic reticulum (ER) makes extensive intermembrane contacts with the plasma membrane (PM), covering ~40% of the PM. Many functions of ER–PM contacts have been proposed, including nonvesicular lipid trafficking, ion transfer, and as signaling hubs. Surprisingly, cells that lack ER–PM contacts grow well, indicating that alternative pathways may be compensating for the loss of ER–PM contact. To better understand the function of ER–PM contact sites we used saturating transposon mutagenesis to identify synthetic lethal mutants in a yeast strain lacking ER–PM contact sites. The strongest hits were components of the ESCRT complexes. The synthetic lethal mutants have low levels of some lipid species but accumulate free fatty acids and lipid droplets. We found that only ESCRT-III components are synthetic lethal, indicating that Vps4 and other ESCRT complexes do not function in this pathway. These data suggest that ESCRT-III proteins and ER–PM contact sites act in independent pathways to maintain lipid homeostasis.**

Monitoring Editor
Mary Munson
University of Massachusetts Medical School

Received: Jan 27, 2020
Revised: Mar 31, 2020
Accepted: Apr 3, 2020

INTRODUCTION

Eukaryotic cells have several layers of organization. The first layer separates the cell from the outside world using a lipid membrane and defines the cell. The second layer of organization is the compartmentalization of the cell by intracellular membranes, generating organelles (Brown *et al.*, 1831; Mullock and Luzio, 2013). The biochemical isolation provided by organelles increases the efficiency of many reactions (Lane and Martin, 2010). The third layer of cellular organization is how organelles are organized within the cell. Membrane contact sites between organelles and other membranes throughout the cell generate an interorganelle network that modulates organelle distribution and morphology (Manford *et al.*, 2012; Helle *et al.*, 2013).

Thin-section electron microscopy allowed researchers to observe and characterize membrane contact sites. The first membrane contact site to be described was between the endoplasmic reticulum (ER) and plasma membrane (PM), described by Porter and Palade in the 1950s (Porter and Palade, 1957). This was only 4 years after the term "endoplasmic reticulum" was first used in a scientific article (Porter and Kallman, 1952). The irony of the term "endoplasmic" was not lost on Palade as he suggested that it would be a "temporary label" and that researchers who wanted a term more descriptive of its morphology "may not have long to wait" (Palade, 1956). Since the 1950s, many contact sites have been described, including nuclear–vacuole (Severs *et al.*, 1976), ER–mitochondria (Copeland and Dalton, 1959), mitochondria–vacuole (Elbaz-Alon *et al.*, 2014), and more (Staehelin, 1997; Raiborg *et al.*, 2015). Membrane contact sites are thought to play important roles in Ca^{2+} signaling, nonvesicular lipid and metabolite transport, mitochondrial dynamics, and interorganelle communication (Friedman *et al.*, 2011; Helle *et al.*, 2013; Omnus *et al.*, 2016). While many of these processes occur at membrane contact sites, studying the role or the essentiality of the proximity of membranes facilitated by membrane contact sites has been challenging; in part, due to the redundancy of tethering proteins (Manford *et al.*, 2012; Quon *et al.*, 2018).

This article was published online ahead of print in MBoC in Press (http://www.molbiolcell.org/cgi/doi/10.1091/mbc.E20-01-0061) on April 8, 2020.

*Address correspondence to: Scott D. Emr (sde26@cornell.edu).

Abbreviations used: DAG, diacylglycerol; ER, endoplasmic reticulum; PC, phosphatidylcholine; PE, phosphatidylethanolamine; PM, plasma membrane; SATAY, saturated transposon analysis in yeast; SL, synthetic lethal; TAG, triacylglycerol.

In yeast, ER–PM contact sites are prolific; nearly 40% of the PM is covered by ER (Manford *et al.*, 2012). At least six protein tethers contribute to ER–PM contact sites: two VAMP-associated proteins (Ssc2/22), three extended synaptotagmins (Tcb1/2/3), and the putative ion channel Ist2 (Manford *et al.*, 2012). Recently, a seventh tether, Ice2, has also been identified (Quon *et al.*, 2018). Deleting six of the ER–PM tethers (generating the Δ*tether* strain, which retains Ice2) dramatically alters ER morphology, induces the unfolded protein response, and changes the distribution and abundance of certain phosphoinositide phosphates (Manford *et al.*, 2012). The loss of ER–PM contact sites, however, only mildly reduced the rate of ergosterol flux between the ER and PM and had little effect on its distribution in cellular membranes (Quon *et al.*, 2018). Surprisingly, the Δ*tether* strain grows well under normal laboratory conditions (Manford *et al.*, 2012). We hypothesized that Δ*tether* cells utilize alternative pathways to adapt to the loss of ER–PM contact sites, which could mask important physiological functions of ER–PM contact sites. The identification and removal of any compensatory pathways could uncover new phenotypes and help our understanding of the function of ER–PM contact sites.

We designed a synthetic lethal (SL) screen to identify compensatory pathways in the Δ*tether* strain. The strain's six deletions made traditional synthetic genetic array analysis too difficult, so we used the saturated transposon analysis in yeast (SATAY) assay (Michel *et al.*, 2017, 2019). The SATAY approach utilizes massive libraries of transposon mutagenized strains. To identify SL genes, we looked for open reading frames (ORFs) that tolerated transposon insertion in the wild-type (WT) strain, but not in the Δ*tether* strain.

The best SL candidates were components of the endosomal sorting complex required for transport (ESCRT) complexes, which are best known for their role in the formation of multivesicular bodies (MVBs). In this pathway, the ESCRTs function sequentially on endosomes; recognizing and sorting cargo (ESCRT-0,I,II), nucleating filament formation (ESCRT-II/III), deforming the membrane to generate vesicles that bud into the endosomal lumen (ESCRT-III), and finally vesicle scission and disassembly of the polymerized complexes (Vps4, an AAA-ATPase; Henne *et al.*, 2011).

The ESCRTs function in many other pathways within the cell. Subsets of ESCRT components function in human immunodeficiency virus budding (Stuchell *et al.*, 2004), cytokinesis (Morita *et al.*, 2007), peroxisomal vesicle budding (Mast *et al.*, 2018), membrane repair (Jimenez *et al.*, 2014), and more (Vietri *et al.*, 2020).

We found that Δ*tether*–ESCRT-III mutants have altered lipid pools; lower levels of phosphatidylserine (PS) and phosphatidylethanolamine (PE), and higher levels of neutral lipids. The Δ*tether*–ESCRT-III mutant growth phenotype can be rescued by shifting the flux of lipid synthesis toward phospholipids and away from neutral lipids. These data indicate that both ER–PM contact sites and ESCRT-III subunits play important roles in maintaining balanced lipid synthesis through distinct pathways.

RESULTS

Identification of genes SL with ER–PM tethers

We used the SATAY screening method to identify SL genes in the Δ*tether* background (Michel *et al.*, 2017, 2019). The SATAY approach utilizes an Ade$^+$ selection to generate massive transposon mutagenized libraries. The density of transposon insertion allowed us to probe whether cells can tolerate a disruption at almost any particular location in the yeast genome. The Ade$^+$ selection is based on a plasmid carrying an inducible transposase and an *ade2* ORF that is disrupted by a transposon. Induction of the transposase removes the transposon from the *ade2* ORF and inserts it randomly into the genome. The cell can then repair the *ade2* ORF, allowing the transposed cells to grow on −ade media. Two SATAY libraries were generated: one in the WT strain background, and one in the Δ*tether* strain background, which has six ER–PM tethers deleted (*tcb1*Δ, *tcb2*Δ, *tcb*3Δ, ist2Δ, scs2Δ, and scs22Δ). Each library contained roughly 2 million Ade$^+$ clones (of which ~60% are transposed), although the transposition efficiency of the Δ*tether* strain was much lower than the WT strain and required harvesting over four times as many plates. The libraries were harvested by scraping all of the cells from transposition plates. The harvested cells were then pooled and outgrown in −ade media to enrich for Ade$^+$ cells.

The transposon insertion sites in both libraries were identified using a next-generation sequencing approach and mapped to the yeast genome using Bowtie2 (Langmead and Salzberg, 2012). The precise site of transposon insertion was determined for each aligned read using a MATLAB script (Michel *et al.*, 2017). In our WT library, we identified 241,160 unique transposon insertions, 84,234 of which fell in ORFs (Figure 1A). Our Δ*tether* library contained 105,351 unique insertions, with 39,958 in ORFs (Figure 1A). Even though each library was generated using a similar number of colonies, the Δ*tether* library contained significantly fewer unique insertions. This was probably due to the disparate colony size in the Δ*tether* library (Supplemental Figure S1A), which could cause small colonies/slower growing cells to be diluted and lost. The disparate colony size may have been due to the strain's low transposition efficency (Δ*tether* transposition plates had ~1/4 the Ade$^+$ colonies per plate compared with WT transposition plates); early transposing cells formed very large colonies that crowded out the later transposing cells.

To identify SL genes, we looked for ORFs that contained relatively fewer transposon insertions in the Δ*tether* library than in the WT library. We plotted each ORF based on the number of transposon insertions in the WT and Δ*tether* libraries (Figure 1B and Supplemental data file 1). ORFs SL with Δ*tether* should appear as outliers below the trendline in the plot in Figure 1B. We initially tested ORFs that had many insertions in the WT library, but none or very few in the Δ*tether* library. To validate outliers as SL with Δ*tether*, we deleted these ORFs in the WT and Δ*tether* backgrounds and tested for synthetic growth phenotypes on rich or synthetic media. None of the initial mutants tested had a growth phenotype. We think this is because our Δ*tether* library was relatively small, and those outliers were either noise or the result of a synthetic lifespan defect without a synthetic growth phenotype. To increase our confidence in SL hits, we looked for groups of genes whose protein products are in the same pathway. This led us to identify the ESCRT complexes as a top hit (Figure 1C). This was unexpected, as the ESCRT complexes primarily function at endosomes to generate MVBs instead of functioning at the ER or PM. Because the ESCRTs are a set of protein complexes (Henne *et al.*, 2011), we decided to delete a core component of each complex in both the WT and the Δ*tether* strain backgrounds to validate the SL phenotype (Figure 1D).

On synthetic media, the ESCRT-III mutant *snf7*Δ had a strong synthetic growth defect in the Δ*tether* strain background (Figure 1D and Supplemental Figure S1, B and C). Other ESCRT-III components also had a growth defect, although it was less severe than the Δ*tether snf7*Δ growth defect (Supplemental Figure S1B). It was very surprising that only components of the ESCRT-III complex were SL in the Δ*tether* strain background, because all known pathways that utilize the ESCRT machinery require more than one complex for function. Additionally, other ESCRT genes like *VPS27* (an ESCRT-0 component), were higher confidence hits having many more insertions in the WT library (33 in *VPS27* vs. 3 in *SNF7*) and none in the Δ*tether* library.

A

SATAY libraries	WT	Δ*tether*
Average Ade+ colonies per plate	22,955	5,226
Estimated colonies harvested (plates)	(90) 2,065,965	(430) 2,246,999
Unique tn insertions	241,160	105,351
tn insertions in ORFs	84,234	39,958

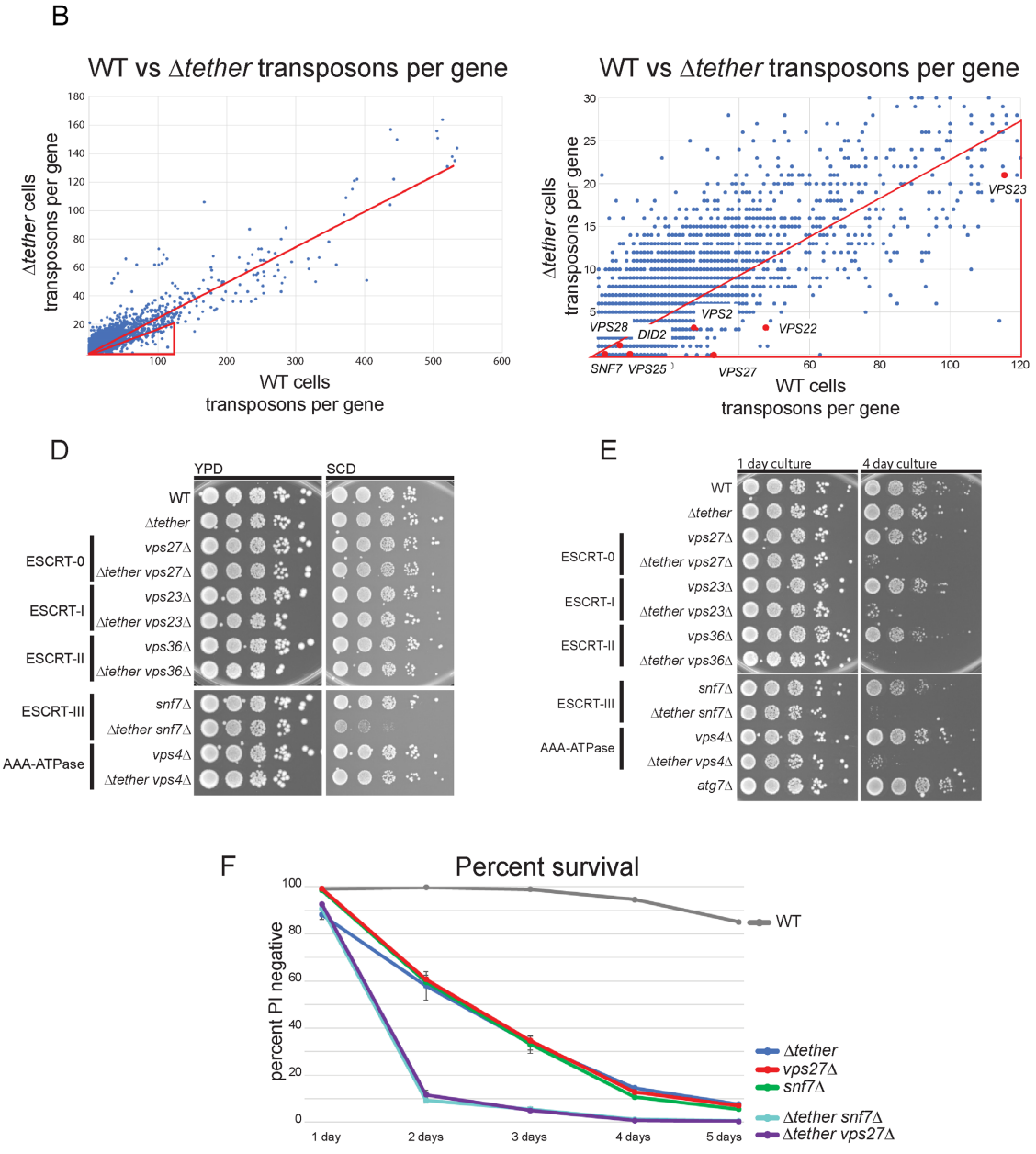

FIGURE 1: The SATAY assay identifies synthetic lethal ORFs. (A) Table showing the number of colonies harvested and transposon insertion sites sequenced in WT and Δ*tether* SATAY libraries. (B) Plot showing each yeast ORF. Each dot represents a different ORF; the position of each ORF was determined by the number of transposon insertions in the WT strain (*x*-axis) and the number of transposon insertions in the Δ*tether* strain (*y*-axis). (C) Close-up view of the plot in Figure 1A. The triangle encompasses ORFs with fewer transposon insertions in the Δ*tether* library compared with the WT library. ORFs encoding ESCRT proteins have been highlighted. (D) Growth assay to validate SATAY hits. Tenfold serial dilutions of WT, Δ*tether*, ESCRT, and Δ*tether* ESCRT mutants were spotted onto YPD and SCD plates. (E) Survival assay to test for reduced chronological lifespan. Cultures were continuously grown in synthetic media for 4 days. Tenfold

The transposition step used for library generation is a 14–18-day incubation on plates, so we reasoned that mutants causing decreased chronological lifespan would also be SATAY hits. To test whether ESCRT mutants caused a chronological lifespan defect in the Δ*tether* strain background, we grew cultures continuously and tested the cells' viability daily. After 4 d of incubation, cells from WT, Δ*tether*, and ESCRT mutant cultures were viable, but ESCRT mutants in the Δ*tether* background were not (Figure 1E). We also stained continuously grown cultures with the membrane impermeant dye propidium iodide (PI), which labels dead cells (Kwolek-Mirek and Zadrag-Tecza, 2014). Δ*tether* and ESCRT mutants died at similar rates, and much faster than WT cells (Figure 1F). ESCRT mutants in the Δ*tether* strain died faster than either ESCRT or Δ*tether* mutants, indicating these mutants are affecting chronological lifespan through different pathways. Mutants from different ESCRT complexes caused similar reductions in chronological lifespan in the Δ*tether* background, unlike the SL growth phenotype, which was only seen in ESCRT-III mutants (Figure 1, D–F). Because both the Δ*tether* strain and ESCRT mutants had relatively short chronological lifespans (Figure 1F), but did not have strong growth defects (Figure 1D), we focused on the synergistic Δ*tether snf7*Δ SL growth phenotype, instead of the more additive Δ*tether* ESCRT mutant chronological lifespan phenotype.

Δtether snf7Δ synthetic lethality is not due to defects in the RIM or MVB pathways

The ESCRT's best characterized function is MVB biogenesis. While all of the ESCRT complexes are required to form MVBs, mutations in different ESCRT complexes can result in intermediate sorting defects on endosomes, which can cause different physiological phenotypes. This is nicely illustrated by the different canavanine sensitivities of early versus late ESCRT mutants (Teis *et al.*, 2010). Early ESCRT mutants allow the canavanine transporter, Can1, to be recycled from endosomes to the PM, while later ESCRT mutants (after *SNF7*) trap and accumulate Can1 on endosomes. To test whether an intermediate sorting defect was responsible for the Δ*tether snf7*Δ SL phenotype, we deleted the ESCRT-0 component *VPS27*. Vps27 is required for recruiting all downstream ESCRTs to the endosome (Katzmann *et al.*, 2003). The growth of the Δ*tether snf7*Δ *vps27*Δ strain was identical to that of the Δ*tether snf7*Δ strain (Supplemental Figure S1D). These data indicate that the Δ*tether snf7*Δ SL phenotype is not due to an intermediate defect in MVB formation.

To identify the Snf7-dependent pathway that is responsible for the Δ*tether snf7*Δ SL phenotype, we looked for ESCRT-dependent pathways that did not require the AAA-ATPase Vps4 or the early ESCRT complexes. The RIM pathway is an alkali response pathway that does not require ESCRT-0 or the ATPase Vps4. The loss of ER–PM tethering has also been shown to activate the RIM pathway and Δ*tether*–RIM mutants have a synthetic phenotype on alkali media (Obara and Kihara, 2017). To test whether defects in the RIM pathway are responsible for the Δ*tether snf7*Δ SL phenotype, we compared the growth phenotypes of Δ*tether vps27*Δ (Vps27 is not required for the RIM pathway, but is for MVB formation), Δ*tether rim20*Δ, and Δ*tether snf7*Δ (Supplemental Figure S1E). Δ*tether rim20*Δ did not phenocopy the Δ*tether snf7*Δ growth defect on synthetic media, indicating that the RIM pathway is not responsible for the Δ*tether snf7*Δ SL growth phenotype. Because all other known ESCRT-mediated pathways require Vps4, these data suggest that Snf7 is acting in a novel pathway that is required for growth in the Δ*tether* strain.

Δtether snf7Δ synthetic lethality is due to a defect in lipid homeostasis

Each of the six ER–PM tethers are implicated in nonvesicular lipid trafficking or ion transport (Loewen and Levine, 2005; Schroeder *et al.*, 2008; Reinisch and De Camilli, 2016). We wanted to test whether the *snf7*Δ SL phenotype was due to the loss of ER–PM membrane proximity, or the loss of the protein tethers and their specific functions. To test this, we used artificial tethers (Omnus *et al.*, 2016; Quon *et al.*, 2018) that restore ER–PM contact but do not have lipid or ion transport activity. While the expression of the ER–PM tethers restored cortical ER (Supplemental Figure S2A), it only minimally rescued the SL growth defect (Figure 2A), indicating that the functions of the tethering proteins are responsible for the SL phenotype and not simply ER–PM membrane proximity.

There are two gene families that make up five of the six ER–PM tethers (*SCS2/22* and *TCB1/2/3*), and the proteins from both families are thought to have lipid transport activity as well as tethering activity (Loewen and Levine, 2005; Reinisch and De Camilli, 2016). To determine whether the nontether function of these protein families is responsible for the *snf7*Δ SL phenotype, we made *snf7*Δ *scs2/22*Δ and *snf7*Δ *tcb1/2/3*Δ strains and compared their growth phenotypes on synthetic media. Both the *snf7*Δ *scs2/22*Δ and the *snf7*Δ *tcb1/2/3*Δ strains had intermediate SL phenotypes, with the *snf7*Δ *scs2/22*Δ phenotype being slightly stronger than the *snf7*Δ *tcb1/2/3*Δ phenotype (Figure 2B). These data suggest that the *snf7*Δ SL phenotype is likely due to general defects in lipid transfer between the ER and PM in the Δ*tether* background, but the pathway in which Snf7 is acting is unknown.

Because rich media suppresses the Δ*tether snf7*Δ growth defect, we thought that identifying the nutrient(s) responsible for suppression could help determine the pathway(s) in which Snf7 is functioning. Because lipid transport activity appears to be critical to the Δ*tether snf7*Δ SL phenotype, we tested the effect of supplementing nutrients that are used for lipid synthesis: serine, choline, and ethanolamine (Figure 2C).

We found that choline and ethanolamine strongly rescue the SL phenotype of Δ*tether snf7*Δ mutants, but serine does not (Figure 2D and Supplemental Figure S2B). Both choline and ethanolamine are substrates of the Kennedy pathway, producing phosphatidylcholine (PC) and PE, respectively (Kennedy and Weiss, 1956). In yeast, PE and PC are primarily made through the CDP-DAG (diacylglycerol) pathway, especially when cells are grown in the absence of exogenous choline or ethanolamine, as is the case in our synthetic media). This indicated that Δ*tether snf7*Δ cells may be accumulating toxic lipid metabolic intermediates or have a defect in PE or PC synthesis.

To examine lipid pools in the Δ*tether snf7*Δ mutant, we preformed lipid extractions on cells grown in synthetic media, and separated the lipids using thin-layer chromatography (Figure 3A).

serial dilutions of equal ODs of cells were spotted on YPD plates after the first and fourth day of culture. (F) Culture viability plot. Samples from continuously grown cultures were stained with propidium iodide (PI) each day for 5 d. The percent of PI-positive cells was determined using flow cytometry. Each spot represents the average of three biological replicates. The error bars represent the SD between the replicates.

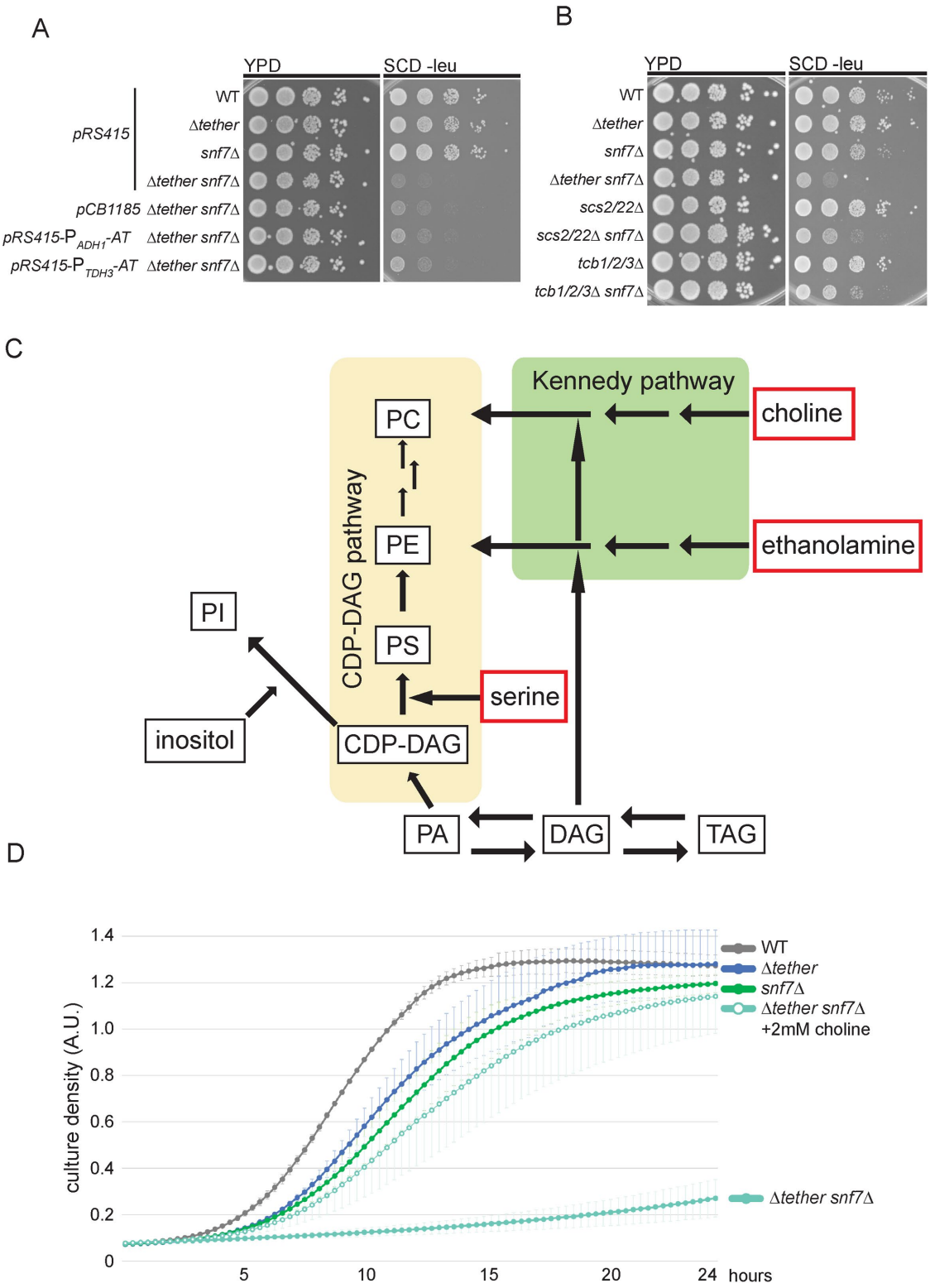

FIGURE 2: Nontethering function of ER–PM tethers is part of the Δ*tether snf7*Δ SL pathway. (A) Growth assay testing artificial ER–PM tethers ability to rescue the Δ*tether snf7*Δ SL phenotype. Tenfold serial dilutions of WT, Δ*tether*, and Δ*tether snf7*Δ strains expressing either an empty vector or an artificial ER–PM tether. Cells were grown overnight in SCD -leu selective media and spotted onto YPD and SCD -leu plates. (B) Growth assay testing for *snf7*Δ SL phenotypes in strains with a subset of ER–PM tethers deleted. Tenfold serial dilutions of Δ*tether snf7*Δ were compared with *scs2/22*Δ *snf7*Δ and *tcb1/2/3*Δ *snf7*Δ, and spotted onto YPD and SCD plates. (C) Simplified lipid synthesis pathway. Nutrients in red boxes are absent in synthetic media. The CDP-DAG pathway is shaded in yellow, and the Kennedy pathway is shaded in green. (D) Growth curve testing the effect of choline supplementation on the Δ*tether snf7*Δ SL growth phenotype. Culture density was detected every 20 min. Each point is the average of three biological replicates; error bars are the SD at each time point.

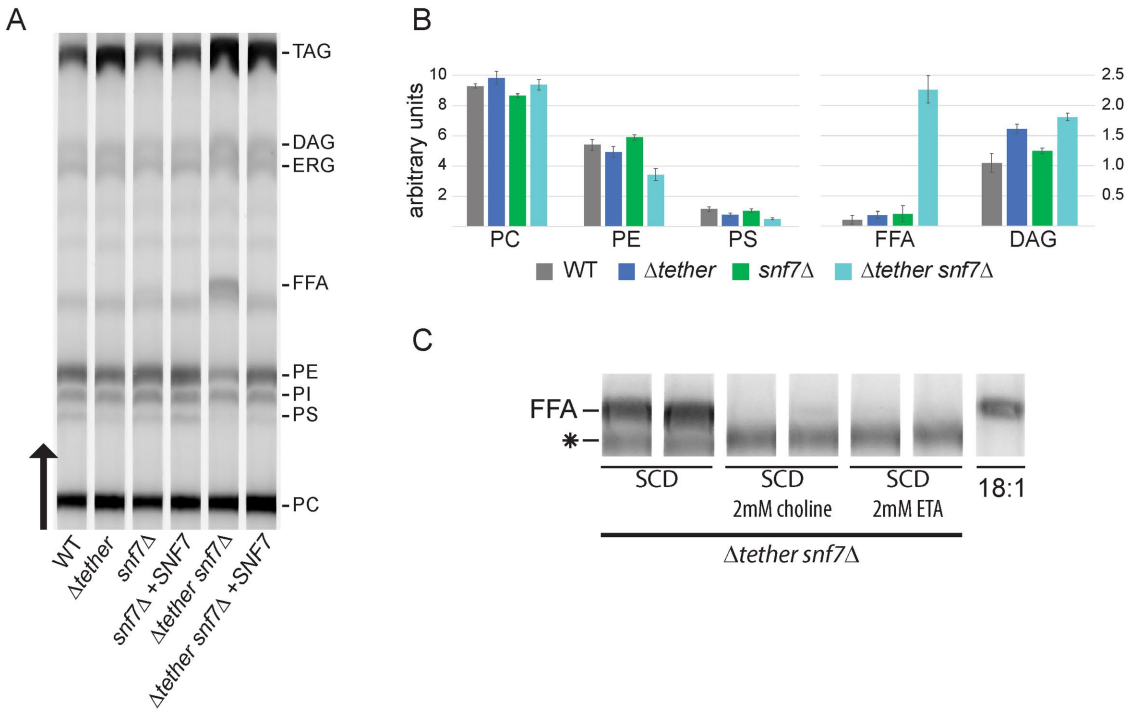

FIGURE 3: Δ*tether snf7*Δ cells have altered lipid pools. (A) TLC separated lipid extracts from WT, Δ*tether*, *snf7*Δ, and Δ*tether snf7*Δ strains. Cells were transformed with an empty vector, or a CEN vector containing *SNF7*. Cells were grown in SCD -ura and harvested at midlog growth phase (OD <1). Lipid extract (10.5 ODE) was loaded from each strain and separated using a two-solvent system. Lipids were visualized using 8-anilino-1-naphthalenesulfonic acid and UV fluorescent imaging. (B) Quantification of lipids from TLC plates. The fluorescence intensity of each lipid species was quantified from three biological replicates. The error bars represent the SD. (C) TLC plate showing lipid extracts from Δ*tether snf7*Δ cells grown in synthetic media supplemented with 2 mM choline, 2 mM ethanolamine, or nothing. Star points to unidentified lipid. Image is cropped from Supplemental Figure 3SA.

We observed several changes in the lipid profiles of Δ*tether snf7*Δ, Δ*tether*, *snf7*Δ, and WT cells. The Δ*tether* strain had lower PS levels, and increased DAG and triacylglycerol (TAG) levels, compared with WT; the *snf7*Δ lipid profile was similar to WT (Figure 3, A and B).

Δ*tether snf7*Δ lipid pools were strikingly altered. PE levels were significantly lower than WT, *snf7*Δ, or Δ*tether* strains. PS levels were also significantly lower than in WT and *snf7*Δ cells, and although not significantly so, PS levels were slightly lower than in Δ*tether* cells. The Δ*tether snf7*Δ lipid samples also contained a strong band that was hardly detectable in WT or the other mutants. This lipid species was identified using mass spectrometry as a mixture of free fatty acids (FFAs), primarily oleic acid. Δ*tether snf7*Δ cells also had increased levels of neutral lipids. Δ*tether snf7*Δ cells had significantly more DAG than control strains as well as increased TAG levels. We found it interesting that PC levels were not significantly altered in the Δ*tether snf7*Δ strain, especially because choline supplementation strongly rescues the SL growth phenotype. As a control, we complemented *snf7*Δ and Δ*tether snf7*Δ strains with *SNF7* and found that the complemented Δ*tether snf7*Δ *SNF7* lipid profile reflected the Δ*tether* lipid profile (Figure 3A).

Choline's effect on lipid species in the Δ*tether snf7*Δ strain

To help make a connection between lipid imbalance and the synthetic growth phenotype of the Δ*tether snf7*Δ strain, we examined the effect of choline supplementation on lipid pools in the Δ*tether snf7*Δ strain. Because choline supplementation rescued the growth defect, choline-induced changes in the lipid profile of the Δ*tether snf7*Δ strain may help to identify potentially toxic or limiting lipids. Choline supplementation influenced the lipid pools of all strains tested. Cells grown with choline had higher levels of PC and slightly lower levels of PE (Supplemental Figure S3A). This indicates that the low PE levels seen in the Δ*tether snf7*Δ strain are not entirely to blame for the SL phenotype. Choline supplementation increased the PS levels in both the Δ*tether* and Δ*tether snf7*Δ strains, but not to WT levels. Choline and ethanolamine supplementation prevented the accumulation of FFAs seen in Δ*tether snf7*Δ cells grown in synthetic media (Figure 3C). Choline supplementation also reduced TAG accumulation in the Δ*tether snf7*Δ strain to similar levels as the Δ*tether* strain. DAG levels were not reduced by choline supplementation; in fact, they were slightly increased. This may indicate that increased DAG levels do not contribute to the SL phenotype; however, we could not tell where in the cell DAG was accumulating, or whether its localization changed after choline supplementation. Because the cells harvested for these experiments were grown in synthetic media (with no exogenous FFAs), the accumulated FFAs are likely the result of lipolysis of neutral lipids, and not from de novo synthesis, as these products should be CoA conjugates. This intimately connects the increased FFA accumulation with increased neutral lipids seen in the Δ*tether snf7*Δ strain and suggests that this strain is overproducing neutral lipids at the expense of phospholipids. The cell may address the lack of phospholipids and accumulated neutral lipids by digesting TAG, generating FFAs, at a rate that the FA-activating enzymes cannot keep up with.

Due to the tight correlation between the growth phenotype and neutral lipid accumulation in the Δ*tether snf7*Δ strain, we examined lipid droplets in cells during midlog growth phase using the fluorescent dye BODIPY 493/503 (Figure 4A). Δ*tether* cells contained

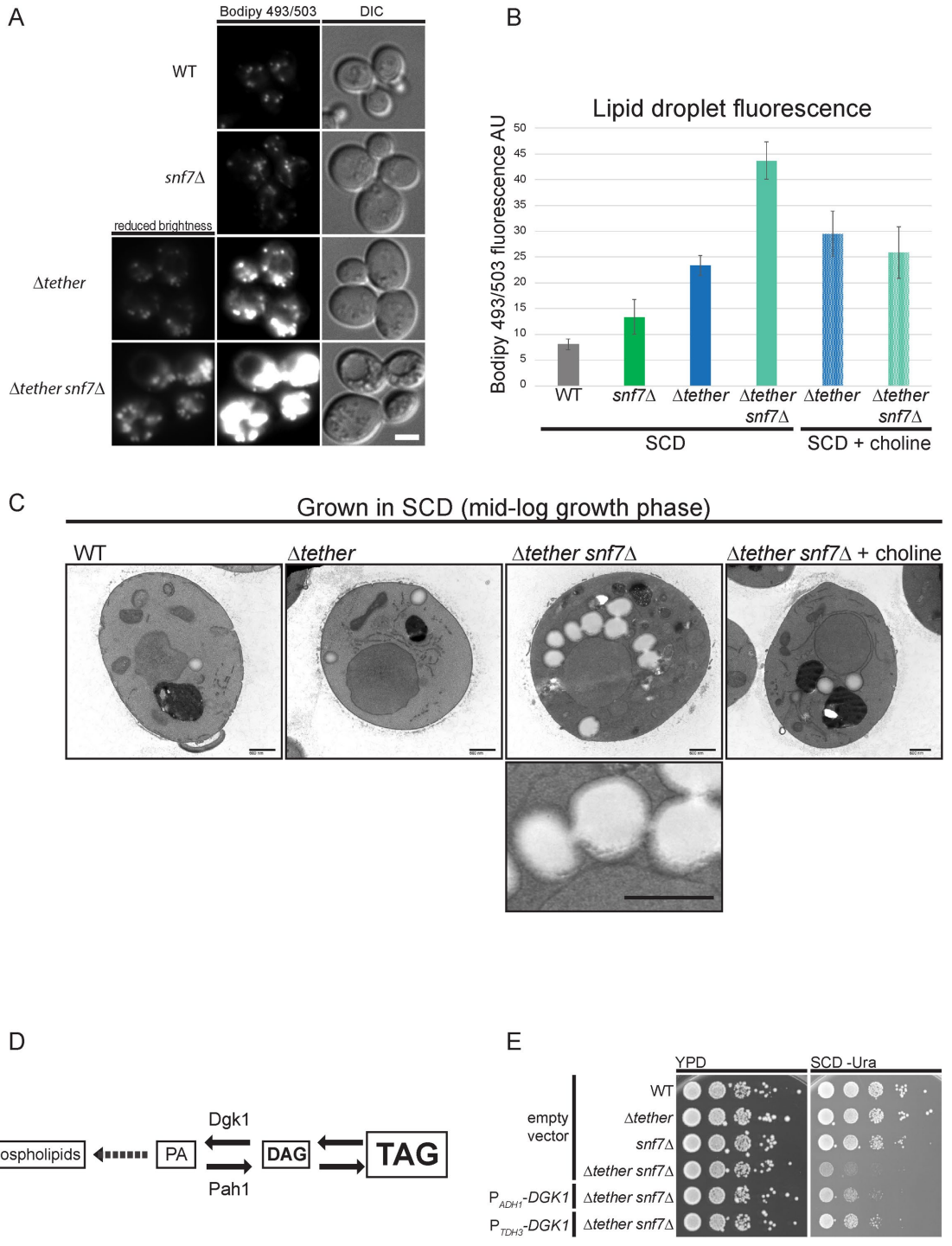

FIGURE 4: Δ*tether snf7*Δ SL growth phenotype is rescued by *DGK1* overexpression. (A) Fluorescence microscopy of cells stained with BODIPY 493/504. Cells were grown in SCD and harvested in midlog growth phase (OD <1). Cells were stained for 10 min with 1.25 µg/ml BODIPY 493/504 in growth media. Cells were washed with 1 ml SCD and imaged using FITC filters. Scale bar is 2 µm. (B) BODIPY 493/504 fluorescence was quantified using flow cytometry. Cells were grown in SCD or SCD supplemented with 2 mM choline and harvested in midlog growth phase (OD <1). Cells were stained for 10 min with 1.25 µg/ml BODIPY 493/504 in growth media. Cells were washed with 1 ml SCD and fluorescence was quantified using a flow cytometer ($n = 4$). Data is presented as mean ± SD. (C) Thin-section electron micrographs of cells harvested in midlog growth phase (OD <1). Cells were grown in SCD or SCD supplemented with 2 mM choline. Scale bar is 600 nm. (D) Model showing regulation of lipid synthesis in yeast. In the Δ*tether snf7*Δ strain lipid synthesis is shifted toward neutral lipids at the expense of phospholipid synthesis. (E) Growth assay testing the SL phenotype of Δ*tether snf7*Δ cells expressing an empty vector or *DGK1* driven by $_{P}$*ADH1* or $_{P}$*TDH3* promoters. Tenfold serial dilutions were spotted on YPD or SCD -ura.

more, and brighter, lipid droplets compared with WT and *snf7*Δ cells. Δ*tether snf7*Δ cells contained even more, and potentially larger, lipid droplets compared with Δ*tether* cells, resulting in a much brighter BODIPY 493/503 signal. We then used flow cytometry to quantify the BODIPY 493/503 fluorescence per cell and found that Δ*tether snf7*Δ cells contained roughly four times the BODIPY 493/503 signal seen in WT cells (Figure 4B). Interestingly, choline supplementation did not affect BODIPY 493/503 fluorescence in Δ*tether* cells, but reduced Δ*tether snf7*Δ lipid droplet fluorescence to that of Δ*tether* cells, negating the *snf7*Δ synthetic effect. Like the mild growth phenotype seen in other ESCRT-III mutants compared with *snf7*Δ in the Δ*tether* background (Supplemental Figure S1B), *vps2*Δ or *vps24*Δ mutations caused a mild increase in BODIPY 493/503 fluorescence in the Δ*tether* background (Supplemental Figure S4).

We used thin-section electron microscopy to determine whether the increased brightness seen after BODIPY 493/503 staining was the result of larger and/or more numerous lipid droplets in the Δ*tether snf7*Δ strain (Figure 4C). The micrographs clearly show that Δ*tether snf7*Δ cells have more and larger lipid droplets than Δ*tether, snf7*Δ, or WT cells. Surprisingly, the lipid droplets in these cells often appear concatenated. Even in thin sections we were able to see chains of up to four lipid droplets, each connected by a narrow neck.

Δ*tether snf7*Δ cells have dysregulated neutral lipid–phospholipid synthesis

In yeast, phosphatidic acid (PA) is the major precursor for phospholipid synthesis, and the lipin Pah1, a PA hydrolase, regulates whether PA goes on to make phospholipids or neutral lipids (Figure 4D; Carman and Han, 2011). It does this by dephosphorylating PA to generate DAG, which is then converted to TAG for storage. Pah1 activity is regulated by phosphorylation; several kinases reduce its phosphatase activity, and one phosphatase complex, Nem1-Spo7, activates it (Carman and Han, 2018). Concatenated lipid droplets have been seen in flies with dysregulated lipin caused by loss of torsin, a lipin activator (Grillet *et al*., 2016). In yeast, overexpression of Nem1-Spo7 induces a proliferation of lipid droplets that are clustered and potentially concatenated (Karanasios *et al*., 2013). These phenotypes suggest that the Δ*tether snf7*Δ SL phenotype may be caused by an imbalance in lipid synthesis; specifically, a dysregulation of enzymes that determine PA and DAG availability. To test this, we overexpressed the DAG kinase *DGK1*. *DGK1* overexpression increases phospholipid synthesis by converting DAG into PA (Han *et al*., 2008). PA is then used as a substrate by the CDP-DAG pathway to generate glycerophospholipids. We overexpressed *DGK1* using two different promoters, the *ADH1* promoter or the *TDH3* promoter, with *TDH3* being the stronger promoter of the two. We found that *DGK1* overexpression rescued the Δ*tether snf7*Δ SL phenotype (Figure 4E). These data indicate that the SL phenotype in Δ*tether snf7*Δ cells is due to excessive neutral lipid synthesis at the expense of phospholipids. The suppression of the SL phenotype by *DGK1* overexpression also indicates that the imbalance in lipid synthesis is occurring at the PA-DAG step and is likely due to hyperactive Pah1 or down-regulated Dgk1.

DISCUSSION

Many important functions have been ascribed to ER–PM contact sites, including ion transport, lipid trafficking, and signaling. In strains that lack ER–PM contact sites, these functions are less diminished than would be expected, and have a negligible impact on growth under normal conditions. We hypothesized that cells lacking ER-PM contact sites could adapt by utilizing alternative pathways to compensate for the loss of ER–PM contact, and that identifying these pathways could help us better understand the function of membrane contact sites. To identify these pathways, we used the SATAY mutagenesis approach, to find genes that are synthetic lethal with Δ*tether*.

Components of the ESCRT complexes were among our top SATAY hits. We initially thought that a defect in MVB formation, and the recycling of lipids in the vacuole, could be responsible for a Δ*tether* ESCRT SL phenotype. After testing components from each of the ESCRT complexes for SL phenotypes, only components of the ESCRT-III complex gave a growth defect in the Δ*tether* background. Because mutations in any of the ESCRT complexes prevent the formation of MVBs, we ruled out vacuolar lipid recycling as the SL pathway.

A subset of ESCRT components function in other pathways inside the cell. These include lipid droplet consumption (Ouahoud *et al*., 2018), peroxisome scission (Mast *et al*., 2018), autophagosome sealing (Takahashi *et al*., 2018), the RIM pathway (Xu *et al*., 2004), CUPS maturation (Curwin *et al*., 2016), nuclear pore complex quality control (Webster *et al*., 2014), and more (Vietri *et al*., 2020). Most of these pathways require the ESCRT-III components and the AAA-ATPase Vps4. Because Δ*tether vps4*Δ cells do not have a SL growth phenotype, we ruled out all of these pathways, except the RIM pathway. The RIM pathway is an alkali response pathway, but has also been shown to be activated by lipid imbalance in the PM. The Δ*tether* strain induces constitutive activation of the RIM pathway, presumably due to changes in the PM lipid content, and Δ*tether RIM* mutants have a synthetic growth defect on alkali media (Ikeda *et al*., 2008; Obara and Kihara, 2017). We showed that Δ*tether rim21*Δ mutants do not have a growth defect on synthetic media, indicating that the RIM pathway is not the SL pathway lost in Δ*tether snf7*Δ mutants (Supplemental Figure S1E). Because Snf7 is required for both the RIM and MVB pathways, we entertained the idea that the Δ*tether snf7*Δ SL phenotype was due to loss of both the RIM and MVB pathways, but ESCRT-I and ESCRT-II mutants, which are required for both pathways, do not have a SL growth phenotype (Figure 1D; Xu *et al*., 2004).

Our genetic evidence indicates that the *snf7*Δ SL pathway is independent of known pathways that use ESCRT components. Snf7 and other ESCRT-III components are filament-forming proteins. Their best characterized function is in membrane deformation, but they are also thought to function as a scaffold in the RIM pathway. ESCRT-III's membrane deformation activity seems to be intimately linked to the AAA-ATPase Vps4, which provides force for scission and/or filament disassembly. This suggests that the *snf7*Δ SL pathway does not utilize Snf7's membrane deforming capacity but instead may be acting as a scaffold that affects regulation or transcriptional control of lipid synthesis pathways.

While several ESCRT-III proteins gave a synthetic growth phenotype in the Δ*tether* strain background, *snf7*Δ was by far the most severe. Although we do not understand the mechanism of Snf7 in lipid homeostasis, we developed two models to describe why different ESCRT-III proteins cause different growth defects in the Δ*tether* background. In the first model, Snf7 is the only protein relevant to lipid homeostasis. Mutations in other ESCRT-III genes cause Snf7 to accumulate on endosomes, reducing the cytoplasmic pool of Snf7 (Teis *et al*., 2008). In this model, cytoplasmic (or nonendosomal) Snf7 regulates lipid synthesis, and the growth defect caused by other ESCRT-III mutants is the result of reduced available Snf7. The major problem with this model is that *vps4*Δ also causes Snf7 to accumulate on endosomes. However, Δ*tether vps4*Δ cells do not have a growth defect like Δ*tether vps2/24*Δ cells

do. In the second model, most ESCRT-III proteins play a role in lipid homeostasis. In this model, *snf7*Δ is more severe than loss of other ESCRT-III proteins because it is the most abundant ESCRT-III protein (Teis *et al.*, 2008).

Δ*tether snf7*Δ mutants produced high levels of neutral lipids, and lower levels of phospholipids. In yeast, the CDP-DAG pathway is the major phospholipid synthesis pathway in the absence of Kennedy pathway substrates. Cells modulate the activity of the CDP-DAG pathway by controlling the availability of its substrate, PA. The PA phosphatase Pah1 dephosphorylates PA, and generates DAG, while the DAG kinase Dgk1 phosphorylates DAG to make PA (Han *et al.*, 2008; Carman and Han, 2018). We found that reducing neutral lipid synthesis by reducing DAG pools suppressed the growth defect in Δ*tether snf7*Δ cells. We did this in two ways; overexpressing *DGK1*, and by stimulating the Kennedy pathway with choline or ethanolamine. The Kennedy pathway consumes DAG by conjugating it to CDP-choline or CDP-ethanolamine (Kennedy and Weiss, 1956).

It is not clear which lipid imbalance is responsible for the Δ*tether snf7*Δ SL phenotype. Choline rescue experiments showed strong reductions in TAG and FAA levels, but did not rescue (and, in fact, exacerbated) the low PE levels. FFAs are cytotoxic, so they could be responsible for the growth defect (Listenberger *et al.*, 2003). The FFAs in Δ*tether snf7*Δ cells are most likely coming from lipolysis because they are grown without exogenous FFAs. We think that the increased neutral lipid synthesis in Δ*tether snf7*Δ cells is resulting in limiting pools of precursors. This in turn leads to high levels of lipolysis of stored neutral lipids, generating FFAs. This may be occurring at a rate that FA-activating enzymes cannot sustain, but it is also possible that the loss of *SNF7* is somehow inhibiting the ability to activate FFAs.

The Δ*tether snf7*Δ SL phenotype is not merely due to the loss of membrane proximity, but instead from the loss of the contact site proteins' function. We found that retethering the ER to the PM in the Δ*tether snf7*Δ strain did little to rescue the growth defect. This brings up an interesting aspect of contact site biology: contact sites are useless without proteins that facilitate some sort of transfer, sensing, or communication between the membranes; and some tethering function is likely inherent in the biology of many of these facilitators. When it comes to the ER–PM contact site, all the tethers are also implicated in functions such as ion transport or lipid transport and are not likely to function solely as tethers. Further, deleting one family of ER–PM tethers (*SCS* or *TCB*) had a modest effect on ER–PM tethering, but did have a *snf7*Δ SL growth defect. Because the Scs and Tcb tethers contain domains implicated in lipid transport, these results suggest that the role of ER–PM contact sites that is important for the *snf7*Δ SL phenotype is lipid transport between the ER and PM.

Our data suggest the following model, which is highly speculative and needs more experimental evidence to be validated, but adequately links the function of ER–PM tethers and Snf7: the Scs and Tcb proteins facilitate transport, or mediate feedback, between the ER and PM. Loss of this transport or feedback results in a defect in the regulation of lipid synthesis. This causes accumulation of neutral lipids, and reduced PS levels in the Δ*tether* strain. Loss of *SNF7* further dysregulates lipid synthesis in the Δ*tether* strain, indicating that Snf7 functions in a backup pathway that can sense lipid pools and regulate lipid synthesis but is distinct from the function of ER–PM contact sites. Our data also suggests that lipid transport at ER–PM contact sites serves to transport specific lipids between the ER and PM to regulate lipid composition, rather than a mechanism to transport lipids in bulk resulting in a large net delivery of lipids to the PM. Because the putative lipid transfer proteins at ER–PM contact sites are not thought to be active transporters, the cell may use them to sense PM lipid pools and regulate lipid synthesis. For example, if the PM concentration of a specific lipid is relatively high, that lipid should not be delivered from the ER to the PM by passive transport. This would result in the accumulation of this lipid in the ER, which can result in activation or repression of ER lipid synthesis enzymes. In cells lacking ER–PM contact sites this feedback would be lost. This is supported by the shift in lipid synthesis toward neutral lipids in the Δ*tether* strain, as well as the ability to suppress the Δ*tether snf7*Δ growth phenotype by manipulating lipid synthesis.

MATERIALS AND METHODS

Media

Standard recipes were used to make yeast extract/peptone/dextrose (YPD) media (Sherman, 2002). Yeast nitrogen base dextrose plates were made using standard recipes (Sherman, 2002), and contained additional nutrients for "complete" plates: adenine (21 mg/ml), histidine (84 mg/ml), leucine (168 mg/ml), lysine (84 mg/ml), methionine (84 mg/ml), tryptofan (84 mg/ml), tyrosine (84 mg/ml), and uracil (84 mg/ml). Dropout plates contained the same additional nutrients as complete plates, except for the dropout nutrient.

The recipe for transposition media was described by the Kornmann lab (https://sites.google.com/site/satayusers/complete-protocol). Transposition media contained 2% galactose (added after autoclaving), yeast nitrogen base, and nutrients (added after autoclaving) at a final concentration of isoleucine (30 mg/ml), valine (150 mg/ml), arginine (20 mg/ml), histidine (20 mg/ml), leucine (100 mg/ml), lysine (30 mg/ml), methionine (20 mg/ml), phenylalanine (50 mg/ml), threonine (200 mg/ml), tryptophan (40 mg/ml), tyrosine (30 mg/ml), uracil (20 mg/ml), glutamic acid (100 mg/ml), and aspartic acid (100 mg/ml).

Choline or ethanolamine was added to plates after autoclaving to a final concentration of 2 mM.

Library generation

Library generation protocol was adapted from the Kornmann lab protocol published online at https://sites.google.com/site/satayusers/complete-protocol. Transposition strains were transformed with pBK549. The transformants were then prescreened after 3–4 d of growth; single colonies were picked and suspended in 200 µl of water and 60 µl was patched onto -ura, -ade, and -ade galactose plates. Patches that gave rise to many colonies on -ade Gal plates, but few on -ade dextrose plates, were chosen to preculture for transposition. Prescreened patches from -ura plates were used to inoculate 250-ml precultures of -ura glucose media to OD600: 0.1. The next day the entire culture was harvested by centrifugation, rinsed with 30 ml -Ade, 2% Gal media, then resuspended at OD_{600}: 35–39. The concentrated cell suspension (200 µl) was spread onto transposition plates using glass beads. The plates were then put into unclosed plastic bags and incubated at 30°C for 15–19 d. During the incubation period, 1-cm squares were drawn on 10% of plates. Periodically the number of colonies within these squares was counted to determine the number of Ade^+ colonies, and the transposition rate. Just before harvesting, the number of Ade^+ colonies was calculated, and roughly 2 million were harvested by adding 2 ml water to each plate and gently scraping the cells from the agar. The harvested cells were inoculated into 2 l -ade glucose media at OD_{600}: 0.2 and grown overnight at 30°C. The next day, the saturated cultures were spun down, rinsed with water, and several 0.5-g pellets were saved in microfuge tubes.

Library DNA extraction

DNA extraction was performed as described here: https://sites.google.com/site/satayusers/complete-protocol/dna-prep.

One 0.5-g cell pellet is resuspended in 500 µl cell breaking buffer (2% Triton X-100, 1% SDS, 100 mM NaCl, 100 mM Tris-HCl, pH 8.0, 1 mM EDTA) and 280 µl was distributed into three microfuge tubes, each containing 300 µl 0.5-mm glass beads. Phenol-chloroform-isoamyl alcohol (PCI; 200 µl; 25:24:1; Invitrogen; 15593031) was added to each tube, and tubes were vortexed for 10 min at 4°C on a vortexer equipped with a foam tube holder (BioExpress; S-7351-24H). TE buffer (200 µl) was then added to each tube, tubes were briefly vortexed, then centrifuged for 5 min at 18,000 × *g*. The upper layer of each tube was transferred to new tubes, 400 µl PCI was added to each tube, and tubes were vortexed for 5 min. Tubes were centrifuged at 18,000 × *g* for 5 min, and the upper layer transferred to new tubes. Chloroform (300 µl) was added to each tube, tubes were vortexed 5 min, and centrifuged at 18,000 × *g* for 5 min. The upper layers were transferred to new tubes. Ethanol (750 µl) was added to each tube, tubes were mixed, then centrifuged 5 min at 18,000 × *g* for 5 min. The supernatant was removed, and pellets were dried. Pellets were resuspended in 200 µl 250 µg/ml RNase A and incubated for 15 min at 55°C while shaking at 1000 rpm on a shaking heat block (Benchmark Multi-Therm Heat–Shake). Each set of three tubes was combined to two tubes (300 µl each). NaOAc, pH 5.2 (30 µl of 3 M) was added to each tube, then mixed. Absolute ethanol (825 µl) was added to each tube to precipitate DNA. Tubes were spun at 18,000 × *g* for 5 min, then the supernatant was removed. DNA pellets were washed with 70% ethanol, and mixed using a TOMY microtube mixer (MT-360) on speed setting 9 for 5 min. The tubes were then centrifuged at 18,000 × *g* for 5 min. The supernatant was aspirated, and the pellets were dried. Each pellet was resuspended in 50 µl water using a shaking heat block at 55°C shaking at 700 rpm. Finally, the DNA from each original pellet was combined.

Digesting library DNA

The DNA concentration was measured by comparing the in-gel fluorescence to a DNA standard curve of DNA ladder (Thermo Scientific GeneRuler DNA ladder). Extracted DNA was diluted 10-fold, and 5 µl of the dilution was loaded on a 1% agarose gel. A standard curve was made by adding 1 µg, 0.8 µg, 0.4 µg, and 0.1 µg of DNA ladder to the same gel. The gel was stained with ethidium bromide after running. The gel was imaged using a Bio-Rad Chemi-doc system, and ImageJ was used to quantify the fluorescence intensity of each lane. The lanes containing extracted library DNA were compared with a standard curve generated by quantifying the fluorescence of the DNA ladder lanes run on the same gel to determine the DNA concentration of the library DNA extractions.

DNA prep for sequencing

The library DNA was digested in two parallel 50-µl reactions; 2 µg of DNA was digested with 50 units of DpnII (NEB R0543S), and 2 µg of DNA was digested with 50 units of NlaIII (NEB R0125S). Both reactions were incubated for 16 h at 37°C. After incubation, the reactions were heat inactivated for 20 min at 65°C. Each digestion (2 µl) was run on a gel to verify digestion.

Each digest was then ligated in 400-µl reactions using 1665 cohesive end ligation units of T4 DNA ligase (NEB M0202L) for 6 h at room temperature.

Ligated DNA was precipitated by adding 40 µl, 3M NaOAc, and 5 µg linear acrylamide (Thermo Fisher; AM9520). After mixing, 1 ml ethanol was added to each tube, and DNA was precipitated at –20°C overnight. DNA was pelleted by centrifuging at 18,000 × *g* at 4°C for 20 min. Pellets were rinsed with 1 ml 70% ethanol, pelleted again by centrifuging at 18,000 × *g* at 4°C for 5 min, and dried. Each pellet was resuspended in 200 µl water on a shaking heat block for 10 min at 55°C and 700 rpm.

Growth assays

Cells were grown to saturation, overnight in YPD (or selective media when plasmids were used). One optical density was collected by centrifugation, rinsed once with water, then resuspended in 1 ml water. This suspension was then serially diluted 10-fold for five dilutions. When cells were carrying a plasmid, cells were grown overnight in selective media with 2 mM choline, then treated as described above. Serial dilutions were applied to plates using a 48-pin replicator. Plates were grown at 30°C for 2–3 d before imaging using an Epson Perfection V600 photo scanner.

Chronological lifespan assay

Cultures were continuously grown in SCD at 30°C. Each day, 1 OD of cells was collected by centrifugation and resuspended in 1 ml water. The suspensions were serially diluted 10-fold for five dilutions and applied to YPD plates using a 48-pin replicator. Plates were grown at 30°C for 2 d.

PI staining and quantification

Cultures were continuously grown in SCD supplemented with 2 mM choline at 30°C. Each day 400 µl of each culture was removed and stained with 1 µg/ml PI for 10 min (in growth media). Samples were centrifuged, and media was aspirated. Each sample was washed with 1 ml fresh media, then resuspended in 250 µl fresh media. A PI-positive control sample was generated by treating cells with 70% EtOH for 5 min before staining.

From each sample, 200 µl was added to 96-well u-bottom plates before being analyzed using an Accuri C6 flow cytometer. Cells (70,000) were measured per sample using the slow setting. Ethanol-treated cells were used to generate a fluorescence threshold to call PI-positive cells. The threshold was set to the FL-2 fluorescence at which >99% but <100% of ethanol-treated cells were at least that fluorescent.

Lipid harvesting

ODs (40–70) of cells growing in midlog growth phase (<OD 1.0) were collected by centrifugation. The pellet was resuspended in 1 ml cold water and transferred to a microcentrifuge tube and centrifuged at 20,000 × *g* for 3 min. The supernatant was aspirated, and the pellet snap-frozen in liquid N_2. Pellets were then stored at –80°C until use.

Lipid extraction

Frozen pellets were resuspended in 1 ml 2:1 (chloroform: methanol) and transferred to a 5-ml glass vial with 400 µl of 0.5-mm zirconia beads. Cells were beat for 10 min on a vortexer equipped with a foam microtube adaptor (BioExpress; S-7351-24H; vials were taped to the foam microtube adaptor). After bead beating, 200 µl 0.034% $MgCl_2$ was added to each vial. Vials were vortexed again for 10 min. Vials were put into 50-ml conical tubes (up to two vials per tube) and centrifuged at 3000 rpm. After centrifugation, the aqueous phase was discarded (~400 µl), and 400 µl pseudo aqueous phase 48:47:3 (methanol: water: chloroform) was added to each vial. Vials were vortexed for 5 min, and centrifuged as described above. The aqueous phase was again discarded, and the organic phase collected in a new vial. The cell lysate was then extracted a second time by adding 400 µl 2:1 (chloroform: methanol) and 200 µl 48:47:3 (methanol: water: chloroform) to each vial. The vials were then vortexed for 10 min. After centrifugation, the aqueous phase was discarded and

the organic phase added to the first extract. The collected organic phase extracts were washed one additional time. Methanol: water: chloroform (48:47:3; 400 µl) was added and vials were vortexed for 5 min. The extracts were transferred to microfuge tubes and centrifuged at 18,000 × *g* for 5 min. The aqueous phase was discarded, and the organic phase collected in a new vial. Finally, the vials were evaporated in a speed vac at 45°C until dry.

Lipid separation/visualization

The lipid extracts were resuspended in 2:1 (chloroform:methanol) at 1.5 ODE/µl. 10.5 ODE (7 µL) of sample was loaded per lane of a TLC plate (Whatman; cat. no. 4865-821). The plate was then placed in a preequilibrated TLC chamber containing solvent I (35:35:40:9; chloroform:trimethylamine:ethanol:water). This solvent was allowed to run 12–14 cm from the origin. The plate was then allowed to dry. Then the plate was placed in a preequilibrated TLC chamber containing solvent II (5:1; isohexane:ethyl-acetate). This solvent was allowed to run to the top of the plate. After drying, the lipids were visualized by spraying the plate with 2.5 mg/ml 8-anilino-1-naphthalenesulfonic acid (Sigma A1028) in 50 mM NaOH. The plate was then imaged using the "stain free gels" program on a Bio-Rad Chemi-Doc MP imaging system.

Quantification of lipid signal

Images of TLC plates were inverted using ImageJ and the band intensity of each lipid species was measured using an ImageJ measure tool. The plate's background fluorescence was determined by measuring the intensity of a lane that had not been loaded with a sample. Samples from three biological replicates were used to generate the quantification. We used the total lipid signal to normalize input between experiments.

BODIPY 493/503 staining and quantification

Midlog growth phase culture (1 ml) was stained with 1.25 µg/ml BODIPY 493/503 for 10 min at room temperature. Cells were spun down and washed once with water and resuspended in 200 µl water. BODIPY fluorescence was quantified using the FL-1 fluorescence on an Accuri C6 flow cytometer. Cells (100,000) from each sample were analyzed using the slow setting.

Electron microscopy

Cells (40 ODs) grown in SCD or SCD + 2 mM choline were harvested form midlog cultures. Cells were fixed in 3% glutaraldehyde, 0.1 M NaCacod, pH 7.4, 5 mM $CaCl_2$, 5 mM $MgCl_2$, 2.5% sucrose for 1 h at room temperature. Cells were washed twice with 0.1 M NaCacod, pH 7.4, and then rinsed with 100 mM Tris, pH 7.6, 25 mM dithiothreitol (DDT), 5 mM EDTA, 1.2 M sorbitol, 25 mM dithiothreitol (DTT). The cell wall was softened by incubating with 100 mM Tris, pH 7.6, 25 mM DDT, 5 mM EDTA, 1.2 M sorbitol, 25 mM DTT for 10 min at room temperature. Cells were then rinsed with spheroplast buffer (0.1 M phosphocitrate, 1 M sorbitol). To spheroplast, cells were resuspended in 0.5 ml spheroplast buffer with 0.25 mg zymolyase and incubated for 30 min. Cells were washed twice with 0.1 M NaCacod, pH 6.8, 5 mM $CaCl_2$. Cells were embedded in 2% ultra-low-melt agarose (50–100 µl), then cut into ~2-mm^3 blocks. Cells were post-fixed/stained in 1% OsO_4, 1% potassium ferrocyanide, 0.1 M NaCacod, pH 6.8, 5 mM $CaCl_2$, 10% formamide for 60 min at room temperature. Blocks were washed four times with water, and then stained with 1% uranyl acetate overnight. Blocks were washed four times with water, and then dehydrated through a graded series of ethanol: 50%, 75%, 95%, 2 × 100% for 10 min each. Blocks were transitioned to propylene oxide incubating blocks in 1:1 propylene oxide:ethanol for 10 min, twice. Blocks were then incubated in 100% propylene oxide for 5 min. The blocks were embedded in 1:1 propylene oxide:epon resin (hard formulation) and left on a rotator overnight to allow the propylene oxide to evaporate. The blocks were transferred to fresh epon resin and polymerized in a 60°C oven for 24 h.

Prepared samples were sectioned at ~70 nM. Sections were poststained with 4% uranyl acetate for 10 min, then Reynold's lead citrate for 2 min (Reynolds, 1963). Images were taken using a Morgagni 268 electron microscope.

ACKNOWLEDGMENTS

We thank Matthew Baile, Lu Zhu, and Sudeep Banjade for critical readings of the manuscript, and Mike Henne, Susan Henry, Maria Laura Gaspar, and Chris Stefan for their stimulating discussions. The Kornmann lab is supported by grants from the Swiss National Science Foundation (Grant no. 31003A_179549) and the Wellcome Trust (Grant no. 214291/Z/18/Z). J.M.B. acknowledges support from the National Institutes of Health (Grant no. R01GM-131101) and the Alfred P. Sloan Foundation (Sloan Research Fellowship). R.T. acknowledges support from a Funai Overseas Fellowship.

REFERENCES

Brown R, Owen R, Royal College of Surgeons of England (1831). Observations On the Organs and Mode of Fecundation in Orchideae and Asclepiadeae. London: Printed by Richard Taylor.

Carman GM, Han G-S (2011). Regulation of phospholipid synthesis in the yeast *Saccharomyces cerevisiae*. Annu Rev Biochem 80, 859–883.

Carman GM, Han G-S (2018). Fat-regulating phosphatidic acid phosphatase: a review of its roles and regulation in lipid homeostasis. J Lipid Res 60, 2–6.

Copeland DE, Dalton AJ (1959). An association between mitochondria and the endoplasmic reticulum in cells of the pseudobranch gland of a teleost. J Biophys Biochem Cytol 5, 393–396.

Curwin AJ, Brouwers N, Alonso Y, Adell M, Teis D, Turacchio G, Parashuraman S, Ronchi P, Malhotra V (2016). ESCRT-III drives the final stages of CUPS maturation for unconventional protein secretion. ELife 5, e16299.

Elbaz-Alon Y, Rosenfeld-Gur E, Shinder V, Futerman AH, Geiger T, Schuldiner M (2014). A dynamic interface between vacuoles and mitochondria in yeast. Dev Cell 30, 95–102.

Friedman JR, Lackner LL, West M, DiBenedetto JR, Nunnari J, Voeltz GK (2011). ER tubules mark sites of mitochondrial division. Science 334, 358–362.

Grillet M, Dominguez Gonzalez B, Sicart A, Pöttler M, Cascalho A, Billion K, Hernandez Diaz S, Swerts J, Naismith TV, Gounko NV, *et al.* (2016). Torsins are essential regulators of cellular lipid metabolism. Dev Cell 38, 235–247.

Han G-S, O'Hara L, Carman GM, Siniossoglou S (2008). An unconventional diacylglycerol kinase that regulates phospholipid synthesis and nuclear membrane growth. J Biol Chem 283, 20433–20442.

Helle SCJ, Kanfer G, Kolar K, Lang A, Michel AH, Kornmann B (2013). Organization and function of membrane contact sites. Biochim Biophys Acta Mol Cell Res 1833, 2526–2541.

Henne WM, Buchkovich NJ, Emr SD (2011). The ESCRT pathway. Dev Cell 21, 77–91.

Ikeda M, Kihara A, Denpoh A, Igarashi Y (2008). The Rim101 pathway is involved in Rsb1 expression induced by altered lipid asymmetry. Mol Biol Cell 19, 1922–1931.

Jimenez AJ, Maiuri P, Lafaurie-Janvore J, Divoux S, Piel M, Perez F (2014). ESCRT machinery is required for plasma membrane repair. Science 343, 1247136.

Karanasios E, Barbosa AD, Sembongi H, Mari M, Han G-S, Reggiori F, Carman GM, Siniossoglou S (2013). Regulation of lipid droplet and membrane biogenesis by the acidic tail of the phosphatidate phosphatase Pah1p. Mol Biol Cell 24, 2124–2133.

Katzmann DJ, Stefan CJ, Babst M, Emr SD (2003). Vps27 recruits ESCRT machinery to endosomes during MVB sorting. J Cell Biol 162, 413–423.

Kennedy EP, Weiss SB (1956). The function of cytidine coenzymes in the biosynthesis of phospholipides. J Biol Chem 222, 193–214.

Kwolek-Mirek M, Zadrag-Tecza R (2014). Comparison of methods used for assessing the viability and vitality of yeast cells. FEMS Yeast Res 14, 1068–1079.

Lane N, Martin W (2010). The energetics of genome complexity. Nature 467, 929–934.
Langmead B, Salzberg SL (2012). Fast gapped-read alignment with Bowtie 2. Nat Methods 9, 357–359.
Listenberger LL, Han X, Lewis SE, Cases S, Farese RV, Ory DS, Schaffer JE (2003). Triglyceride accumulation protects against fatty acid-induced lipotoxicity. Proc Natl Acad Sci USA 100, 3077–3082.
Loewen CJR, Levine TP (2005). A highly conserved binding site in vesicle-associated membrane protein-associated protein (VAP) for the FFAT motif of lipid-binding proteins. J Biol Chem 280, 14097–14104.
Manford AG, Stefan CJ, Yuan HL, MacGurn JA, Emr SD (2012). ER-to-plasma membrane tethering proteins regulate cell signaling and ER morphology. Dev Cell 23, 1129–1140.
Mast FD, Herricks T, Strehler KM, Miller LR, Saleem RA, Rachubinski RA, Aitchison JD (2018). ESCRT-III is required for scissioning new peroxisomes from the endoplasmic reticulum. J Cell Biol 217, 2087–2102.
Michel AH, Hatakeyama R, Kimmig P, Arter M, Peter M, Matos J, De Virgilio C, Kornmann B (2017). Functional mapping of yeast genomes by saturated transposition. ELife 6, e23570.
Michel AH, van Schie S, Mosbach A, Scalliet G, Kornmann B(2019). Exploiting homologous recombination increases SATAY efficiency for loss- and gain-of-function screening. BioRxiv 866483.
Morita E, Sandrin V, Chung H-Y, Morham SG, Gygi SP, Rodesch CK, Sundquist WI (2007). Human ESCRT and ALIX proteins interact with proteins of the midbody and function in cytokinesis. EMBO J 26, 4215–4227.
Mullock BM, Luzio JP (2013). Theory of organelle biogenesis: a historical perspective. In: The Biogenesis of Cellular Organelles, ed. C Mullins, Boston, MA: Springer US, 1–18.
Obara K, Kihara A (2017). The Rim101 pathway contributes to ER stress adaptation through sensing the state of plasma membrane. Biochem J 474, 51–63.
Omnus DJ, Manford AG, Bader JM, Emr SD, Stefan CJ (2016). Phosphoinositide kinase signaling controls ER-PM cross-talk. MBoC 27, 1170–1180.
Ouahoud S, Fiet MD, Martínez-Montañés F, Ejsing CS, Kuss O, Roden M, Markgraf DF (2018). Lipid droplet consumption is functionally coupled to vacuole homeostasis independent of lipophagy. J Cell Sci 131, jcs213876.
Palade GE (1956). The endoplasmic reticulum. J Biophys Biochem Cytol 2, 85–98.
Porter KR, Kallman FL (1952). Significance of cell particulates as seen by electron microscopy. Ann NY Acad Sci 54, 882–891.
Porter KR, Palade GE (1957). Studies on the endoplasmic reticulum. III. Its form and distribution in striated muscle cells. J Biophys Biochem Cytol 3, 269–300.
Quon E, Sere YY, Chauhan N, Johansen J, Sullivan DP, Dittman JS, Rice WJ, Chan RB, Paolo GD, Beh CT, *et al*. (2018). Endoplasmic reticulum-plasma membrane contact sites integrate sterol and phospholipid regulation. PLOS Biol 16, e2003864.
Raiborg C, Wenzel EM, Stenmark H (2015). ER–endosome contact sites: molecular compositions and functions. EMBO J 34, 1848–1858.
Reinisch KM, De Camilli P (2016). SMP-domain proteins at membrane contact sites: structure and function. Biochim Biophys Acta 1861, 924–927.
Reynolds ES (1963). The use of lead citrate at high pH as an electron-opaque stain in electron microscopy. J Cell Biol 17, 208–212.
Schroeder BC, Cheng T, Jan YN, Jan LY (2008). Expression cloning of TMEM16A as a calcium-activated chloride channel subunit. Cell 134, 1019–1029.
Severs NJ, Jordan EG, Williamson DH (1976). Nuclear pore absence from areas of close association between nucleus and vacuole in synchronous yeast cultures. J Ultrastruct Res 54, 374–387.
Sherman F (2002). Getting started with yeast. Meth Enzymol 350, 3–41.
Staehelin LA (1997). The plant ER: a dynamic organelle composed of a large number of discrete functional domains. Plant J 11, 1151–1165.
Stuchell MD, Garrus JE, Müller B, Stray KM, Ghaffarian S, McKinnon R, Kräusslich H-G, Morham SG, Sundquist WI (2004). The human endosomal sorting complex required for transport (ESCRT-I) and its role in HIV-1 budding. J Biol Chem 279, 36059–36071.
Takahashi Y, He H, Tang Z, Hattori T, Liu Y, Young MM, Serfass JM, Chen L, Gebru M, Chen C, *et al*. (2018). An autophagy assay reveals the ESCRT-III component CHMP2A as a regulator of phagophore closure. Nat Commun 9, 1–13.
Teis D, Saksena S, Emr SD (2008). Ordered assembly of the ESCRT-III complex on endosomes is required to sequester cargo during MVB formation. Dev Cell 15, 578–589.
Teis D, Saksena S, Judson BL, Emr SD (2010). ESCRT-II coordinates the assembly of ESCRT-III filaments for cargo sorting and multivesicular body vesicle formation. EMBO J 29, 871–883.
Vietri M, Radulovic M, Stenmark H (2020). The many functions of ESCRTs. Nat Rev Mol Cell Biol 21, 25–42.
Webster BM, Colombi P, Jäger J, Lusk CP (2014). Surveillance of nuclear pore complex assembly by ESCRT-III/Vps4. Cell 159, 388–401.
Xu W, Smith FJ, Subaran R, Mitchell AP (2004). Multivesicular body-ESCRT components function in pH response regulation in *Saccharomyces cerevisiae* and *Candida albicans*. Mol Biol Cell 15, 5528–5537.